Hubble Space Telescope Hα imaging of star-forming galaxies at $z \simeq$ 1–1.5: evolution in the size and luminosity of giant H II regions

R. C. Livermore,[1⋆] T. Jones,[2] J. Richard,[1,3] R. G. Bower,[1] R. S. Ellis,[2]
A. M. Swinbank,[1] J. R. Rigby,[4] Ian Smail,[1] S. Arribas,[5] J. Rodriguez-Zaurin,[6]
L. Colina,[5] H. Ebeling[7] and R. A. Crain[8]

[1]*Institute for Computational Cosmology, Durham University, South Road, Durham DH1 3LE*
[2]*Astronomy Department, California Institute of Technology, MC 249-17, Pasadena, CA 91125, USA*
[3]*CRAL Observatoire de Lyon, 9 Avenue Charles André, 69561 Saint-Genis-Laval, France*
[4]*NASA Goddard Space Flight Center, Code 665, Greenbelt, MD 20771, USA*
[5]*Centro de Astrobiologia, Departamento de Astrofísica, CSIC-INTA, Ctra. de Ajalvir km. 4, 28850 Torrejón de Ardoz, Madrid, Spain*
[6]*Instituto de Astrofísica de Canarias (IAC), C/Via Láctea s/n, E38205, La Laguna, Tenerife, Spain*
[7]*Institute for Astronomy, University of Hawaii, 2680 Woodlawn Drive, Honolulu, HI 96822, USA*
[8]*Leiden Observatory, Leiden University, PO Box 9513, 2300 RA Leiden, the Netherlands*

ABSTRACT

We present *Hubble Space Telescope*/Wide Field Camera 3 narrow-band imaging of the Hα emission in a sample of eight gravitationally lensed galaxies at $z = 1$–1.5. The magnification caused by the foreground clusters enables us to obtain a median source plane spatial resolution of 360 pc, as well as providing magnifications in flux ranging from ∼10× to ∼50×. This enables us to identify resolved star-forming H II regions at this epoch and therefore study their Hα luminosity distributions for comparisons with equivalent samples at $z \sim 2$ and in the local Universe. We find evolution in the both luminosity and surface brightness of H II regions with redshift. The distribution of clump properties can be quantified with an H II region luminosity function, which can be fit by a power law with an exponential break at some cut-off, and we find that the cut-off evolves with redshift. We therefore conclude that 'clumpy' galaxies are seen at high redshift because of the evolution of the cut-off mass; the galaxies themselves follow similar scaling relations to those at $z = 0$, but their H II regions are larger and brighter and thus appear as clumps which dominate the morphology of the galaxy. A simple theoretical argument based on gas collapsing on scales of the Jeans mass in a marginally unstable disc shows that the clumpy morphologies of high-z galaxies are driven by the competing effects of higher gas fractions causing perturbations on larger scales, partially compensated by higher epicyclic frequencies which stabilize the disc.

Key words: gravitational lensing: strong – galaxies: high-redshift – galaxies: star formation.

1 INTRODUCTION

Observations of star-forming galaxies at high-z have shown that a significant fraction of the population has turbulent, clumpy, rotating discs with clump masses of $\sim 10^{8-9}$ M$_\odot$, a factor of $\sim 100\times$ the typical giant molecular cloud (GMC) locally (e.g. Cowie, Hu & Songaila 1995; Elmegreen et al. 2004, 2009; Elmegreen & Elmegreen 2005; Förster Schreiber et al. 2009). The clumps are thought to form from gravitational instabilities in gas-rich discs (Elmegreen et al. 2007, 2009; Genzel et al. 2008; Bournaud et al. 2010).

Some recent numerical simulations have suggested that the majority of massive, high-z galaxies accrete their gas via 'cold flows',

in which the gas is accreted smoothly along filaments. These cold flows are less disruptive than a major merger, and hence offer a route to maintain marginally stable discs (Toomre parameter $Q \sim 1$) without disrupting the structure and dynamics. Cold-flow accretion is expected to be a dominant mode of mass assembly above $z \simeq 1$, and thus accounts for the ubiquity of large clumps at high redshift (e.g. Bournaud & Elmegreen 2009; Dekel, Sari & Ceverino 2009; Bournaud et al. 2011).

In this picture, the clumps are considered to be transient features, forming in marginally unstable discs at high-z and fed by smooth accretion of gas on to the galaxy. Clumpy galaxies therefore represent a phase in the evolution of present-day spiral discs.

There is a need to test the internal physical properties of the interstellar medium (ISM) observationally to determine whether the clumps are scaled-up analogues of local H II regions or represent a

⋆E-mail: r.c.livermore@durham.ac.uk

different 'mode' of star formation, and whether they can explain the strong evolution of star formation rate (SFR) density with redshift. However, sufficient spatial resolution is required to resolve the ISM on the scales of star-forming regions. Even with the use of adaptive optics, spatially resolved studies of high-redshift galaxies to date have been limited to a resolution of ∼1.5 kpc (e.g. Genzel et al. 2006; Förster Schreiber et al. 2009); using the *Hubble Space Telescope* (*HST*), only the largest starburst complexes can be resolved, on scales of ∼1 kpc (Elmegreen et al. 2007). On these scales, it is possible to probe the dynamics of galaxies on large scales, and Genzel et al. (2011) found evidence that $Q < 1$ in the regions of galaxies where clumps are found, lending observational support to the theory that the clumps form from internal gravitational instabilities. In order to study the clumps in detail, we need to resolve high-redshift discs on the scales of individual star-forming regions; in the local universe, this is ∼100 pc.

The required spatial resolution can currently only be achieved by exploiting gravitational lensing. By targeting galaxies that lie behind foreground cluster lenses, it is possible to benefit from linear magnification factors (along one direction) of up to 50× (e.g. Swinbank et al. 2007, 2009; Jones et al. 2010), and to isolate H II regions of order ∼100 pc out to $z \sim 5$ (Swinbank et al. 2009). Regions were found with star formation surface densities $\Sigma_{SFR} \sim 100\times$ higher than those found locally (Swinbank et al. 2009; Jones et al. 2010). These regions of dense star formation are comparable to the most intensely star-forming interacting systems in the local Universe (Bastian et al. 2006), yet appear to be ubiquitous in non-interacting galaxies at high redshift.

It is not known what drives these regions of intense star formation at high-z, although Jones et al. (2010) suggest a combination of higher gas density, increased star formation efficiency and shorter star formation time-scales. In addition, their data give the appearance of a bimodal distribution of H II region surface brightnesses, although there is no known physical process that might drive this. In order to understand this result further, we require a sample at intermediate redshift ($z \sim 1$–1.5) with which we can probe the evolution of star formation density with redshift at higher sensitivity so that regions comparable to those at $z = 0$ are detectable.

Previous work on high-z clumps has made use of integral field units such as Keck/OH-Suppressing Infrared Integral Field Spectrograph (OSIRIS; Jones et al. 2010; Wisnioski et al. 2012),

Gemini/Near-Infrared Integral Field Spectrometer (NIFS; Swinbank et al. 2009) and Very Large Telescope (VLT)/Spectrograph for Integral Field Observations in the Near Infrared (SINFONI; Förster Schreiber et al. 2009). These allow detailed mapping of the nebular emission lines, but at lower sensitivity than is achievable with imaging. An alternative means of identifying star-forming regions with high sensitivity is to take imaging through narrow-band filters. The Wide Field Camera 3 (WFC3) on the *HST* presents an opportunity to study the star formation in galaxies at $z \sim 1$ and ∼1.5, as there are narrow-band filters available which correspond to the wavelength of the Hα emission line at these redshifts. Combining the sensitivity and high spatial resolution of *HST*/WFC3 with the magnification afforded by gravitational lensing by foreground clusters, we can map the internal star formation distribution and so identify the frequency and properties of giant H II regions.

In this paper, we therefore study the star formation morphologies of eight galaxies at $z \sim 1$–1.5. We present the sample in Section 2, present the properties of the galaxies and their star-forming clumps in Section 3, discuss the implications in Section 4 and present our conclusions in Section 5. Throughout, we adopt a Λ cold dark matter (ΛCDM) cosmology with $H_0 = 70 \, \text{km s}^{-1} \, \text{Mpc}^{-1}$, $\Omega_\Lambda = 0.7$ and $\Omega_m = 0.3$. SFRs are calculated from Hα luminosity $L_{H\alpha}$ using the prescription of Kennicutt (1998a) adjusted to a Chabrier (2003) initial mass function (IMF).

2 SAMPLE AND OBSERVATIONS

Our sample comprises eight lensed galaxies, each with spectroscopically confirmed redshifts in the range $1 < z < 1.5$ such that the Hα emission line falls within the high-transmission region of the narrow-band filters on WFC3. The associated cluster lenses are massive systems from the X-ray selected Brightest Cluster Sample (BCS) and Massive Cluster Survey (MACS) samples (Ebeling et al. 1998, 2007, 2010; Ebeling, Edge & Henry 2001) with well-constrained mass models (see references in Table 1), so that the effects of lensing can be accounted for.

The positions and properties of the sample are given in Table 1. We observed each target in the narrow-band filter covering Hα for a typical exposure time of 6 ks (2 orbits), using a 3- or 4-point linear dithering pattern of ±5 arcsec in both directions to improve

Table 1. Properties of the redshift-selected sample. Lensing magnifies the image by a factor μ_x at a position angle (PA), with a transverse magnification μ_y. The total magnification factor μ is calculated from the amplification of Hα flux, and the resolution given is the highest achievable along the most magnified direction, calculated from the FWHM of a star under the same lensing transformation as that applied to the galaxy, as described in the text. All observations were obtained under Program 12197 (Cycle 18, PI: Richard) unless otherwise stated.

Target cluster	Arc position RA (J2000)	Dec. (J2000)	z	Hα flux (intrinsic) (10^{-18} erg s^{-1} cm^{-2})	Magnification $\mu_x \times \mu_y$ (PA)	μ	Resolution (pc)	Broad-band filter	Narrow-band filter	Lens model reference
Abell 611	08:00:57.30	+36:03:37.0	0.908	30 ± 5	10.4 × 2.7 (1°)	28 ± 5	338	*F125W*[a]	*F126N*	[1]
Abell 2390	21:53:34.55	+17:42:02.4	0.912	39 ± 6	5.5 × 2.3 (73°)	12.6 ± 1.9	435	*F125W*[b]	*F126N*[b]	[2]
Abell 773	09:17:58.80	+51:43:42.3	1.010	274 ± 49	7.0 × 1.0 (61°)	7 ± 1	336	*F110W* *F160W*[c]	*F132N*	[1]
MACS J0947.2+7623	09:47:15.26	+76:23:02.9	1.012[d]	8.5 ± 2.2	3.0 × 17.7 (51°)	53 ± 14	172	*F125W*	*F132N*	[3]
Abell 68	00:37:04.91	+09:10:21.0	1.017	119 ± 11	3.0 × 1.7 (41°)	5.1 ± 0.5	615	*F110W* *F160W*[e]	*F132N*	[4]
MACS J0159.8−0849	01:59:04.68	-34:13:03.4	1.488[e]	7 ± 1	10.7 × 3.0 (111°)	32 ± 4	592	*F160W*	*F164N*	[3]
MACS J1149.5+2223	11:49:35.30	+22:23:45.8	1.490[f]	11 ± 2	4.5 × 3.5 (140°)	15 ± 3	315	*F160W*[b]	*F164N*	[5]
MACS J1133.2+5008	11:33:14.31	+50:08:39.7	1.550	8 ± 1	1.1 × 12.7 (67°)	14 ± 2	68	*F160W*	*F167N*	[6]

[a]Program 12065-9; [b]Program 11678; [c]Program 11591; [d]Ebeling et al. (2010); [e]Ebeling et al. (in preparation); [f]Ebeling et al. (2007).
References: [1] Richard et al. (2010); [2] Pello et al. (1991); [3] Richard et al. (in preparation); [4] Richard et al. (2007); [5] Smith et al. (2009); [6] Sand et al. (2005).

the detection and removal of cosmic ray hits and bad pixels. At the same time, three of the targets (MACS J0947, MACS J0159 and MACS J1133), which did not have WFC3 data in the archive, were observed in the corresponding broad-band filter using the same sequence of observations as their corresponding narrow-band data, for a total of 3 ks (1 orbit). The narrow-band data and new broad-band observations were obtained in Cycle 18 under Program 12197 (PI: Richard), with the exception of Abell 2390, for which the broad-band and narrow-band data were taken in Cycle 17 under Program 11678 (PI: Rigby). The remaining broad-band data were obtained under Cycle 17 Program 11591 (PI: Kneib) or Cycle 18 Program 12065-9 (PI: Postman) as indicated in the notes to Table 1.

All of the WFC3 data were reduced using the MULTIDRIZZLE software (Koekemoer et al. 2002) under PYRAF to perform a cosmic ray rejection, sky subtraction and drizzling on to an output pixel scale of 0.05 arcsec. The narrow-band and broad-band images of the same cluster were aligned using the location of ∼20 bright stars. A narrow-band excess image was constructed by direct pixel-to-pixel subtraction between the narrow-band and broad-band images, including an arbitrary scaling factor. We calibrated this scaling factor by checking that all bright cluster members, which are featureless elliptical galaxies with no emission lines in the respective filters, became consistent with the background in the excess image. For Abell 773 and Abell 68, the broad-band images available in the archive did not directly overlap the Hα emission line, so an estimate of the broad-band continuum was made by linear interpolation between the adjacent *F110W* and *F160W* filters.

The flux calibration of each image was verified using Two Micron All Sky Survey (2MASS) stars in the fields, and in all cases was found to agree to within 15 per cent, which is sufficient precision for our purposes.

Colour *HST* images of the clusters are shown in Fig. 1, with the critical lines at the redshift of the target arc overlaid. We use the transformation between image and source plane mapping from the best-fitting cluster mass models (for details of the mass models, see references in Table 1) with LENSTOOL (Kneib 1993; Jullo et al. 2007) to reconstruct the images in the source plane, and show these in Fig. 2. In order to reconstruct the source plane morphology, LENSTOOL uses the mapping between the image and source planes on a cluster-by-cluster basis and ray traces the galaxy image. The lensing effect is to stretch the galaxy image – in most cases along one direction – and so the reconstruction cannot 'create' new H II regions, but rather the lensing has acted to extend them. As surface brightness is conserved by lensing, we then apply this conservation to obtain the intrinsic source plane flux. The total magnification is then simply the ratio of the image- to source plane flux. To obtain the errors on the magnification, we use the family of best-fitting lens models which adequately describe the cluster potential, derived by sampling the posterior probability distribution of each parameter of the model (see Richard et al. 2010 for more details). For each acceptable lens model, we reconstruct the arc and remeasure the amplification. We give the resulting magnification factors, μ, and associated errors in Table 1.

In cases where the target is multiply imaged, the images were reconstructed separately and then adjusted for small differences in position and orientation before being combined. For MACS J0159, which consists of five images, only the first three were used due to the high magnification gradients in the fourth and fifth images resulting in high distortion in the source plane reconstructions. In the case of Abell 611, we use only the northernmost arc due to high distortion by a foreground galaxy lying close to the line of sight of the southern arc.

We derive total magnification factors by comparing the total luminosities of the image- and source plane Hα excess images. The intrinsic Hα luminosities are in the range 0.45–15×10^{41} erg s^{-1} corresponding to SFRs of 0.4–$12 \, M_\odot$ yr^{-1}. These are at the faint end of the Hα luminosity function (LF) for this redshift range (see Fig. 3), and probe fainter galaxies than the $z \sim 2$ sample of Jones et al. (2010), which covers the range 2.5–32×10^{41} erg s^{-1}, although the two samples overlap in luminosity. Because of the increased sensitivity provided by the lensing magnification, both of the lensed samples cover a lower range of intrinsic Hα luminosities than the sample of Spectroscopic Imaging Survey in the Near-Infrared with SINFONI (SINS) galaxies studied by Förster Schreiber et al. (2011b), which were selected to have bright Hα and lie in the range 28–43×10^{41} erg s^{-1}, making them rare, intensely star-forming galaxies. Thus, by harnessing gravitational lensing we are able to probe the more 'normal' star-forming population.

Since gravitational lensing can preferentially shear one direction, we estimate the effective source plane resolution by reconstructing the image of a star from the field repositioned to lie at the centre of the target. The maximum linear resolution, derived from the full width at half-maximum (FWHM) of the reconstructed star in the direction of greatest magnification, is 68–615 pc with a median of 360 pc, sufficient to resolve giant H II regions.

2.1 Comparison samples

In order to interpret our high-z data, we exploit the Hα narrow-band imaging from the *Spitzer* Infrared Nearby Galaxies Survey (SINGS; Kennicutt et al. 2003), which comprises Hα imaging of 75 galaxies with corrected SFRs of up to 11 $M_\odot$ yr^{-1}. We use the publicly available continuum-subtracted Hα narrow-band imaging and restrict the sample to those with Hα detections with signal-to-noise ratio of >5 that have no significant defects in the galaxy images (determined by visual inspection). This restricts the SINGS sample to 41 galaxies with SFR > $4 \times 10^{-4} \, M_\odot$ yr^{-1}.

To ensure a fair comparison, we rebin the SINGS images so that the resolution is comparable to the high-z data and then threshold to the median surface brightness limit of the $z \sim 1$–1.5 observations. It is worth noting that thresholding the images in this manner excludes 10–50 per cent of the total star formation. This should not affect the comparison between samples which have the same surface brightness limit, but may serve as an indication of the fraction of star formation missed in high-z observations.

To provide a comparison to local galaxies which are more actively star forming, we use the Visible Multi-Object Spectrograph (VIMOS) Hα imaging spectroscopy of Rodríguez-Zaurín et al. (2011), which includes 38 luminous infrared galaxies (LIRGs) and ultraluminous infrared galaxies (ULIRGs) at $z < 0.13$ with spatial resolution of 130–1.2 kpc and SFR $\lesssim 25 \, M_\odot$ yr^{-1}.

We also compare the $z \sim 1$–1.5 sample to the $z \sim 2$ lensed arcs of Jones et al. (2010), which were observed with Keck/OSIRIS. In order to provide a fair comparison, we have constructed narrow-band images by summing the OSIRIS cubes over 100 Å either side of the redshifted Hα emission line, matching the width of the WFC3 narrow-band filters. The resulting images are then corrected for lensing using the same image-to-source plane mapping as Jones et al. (2010) in order to obtain the intrinsic galaxy properties.

2.2 Determination of galaxy properties

The total Hα luminosities of the galaxies in all samples are determined by summing all pixels in sky-subtracted images with signal-to-noise ratio of >3. In the case of the SINGS galaxies,
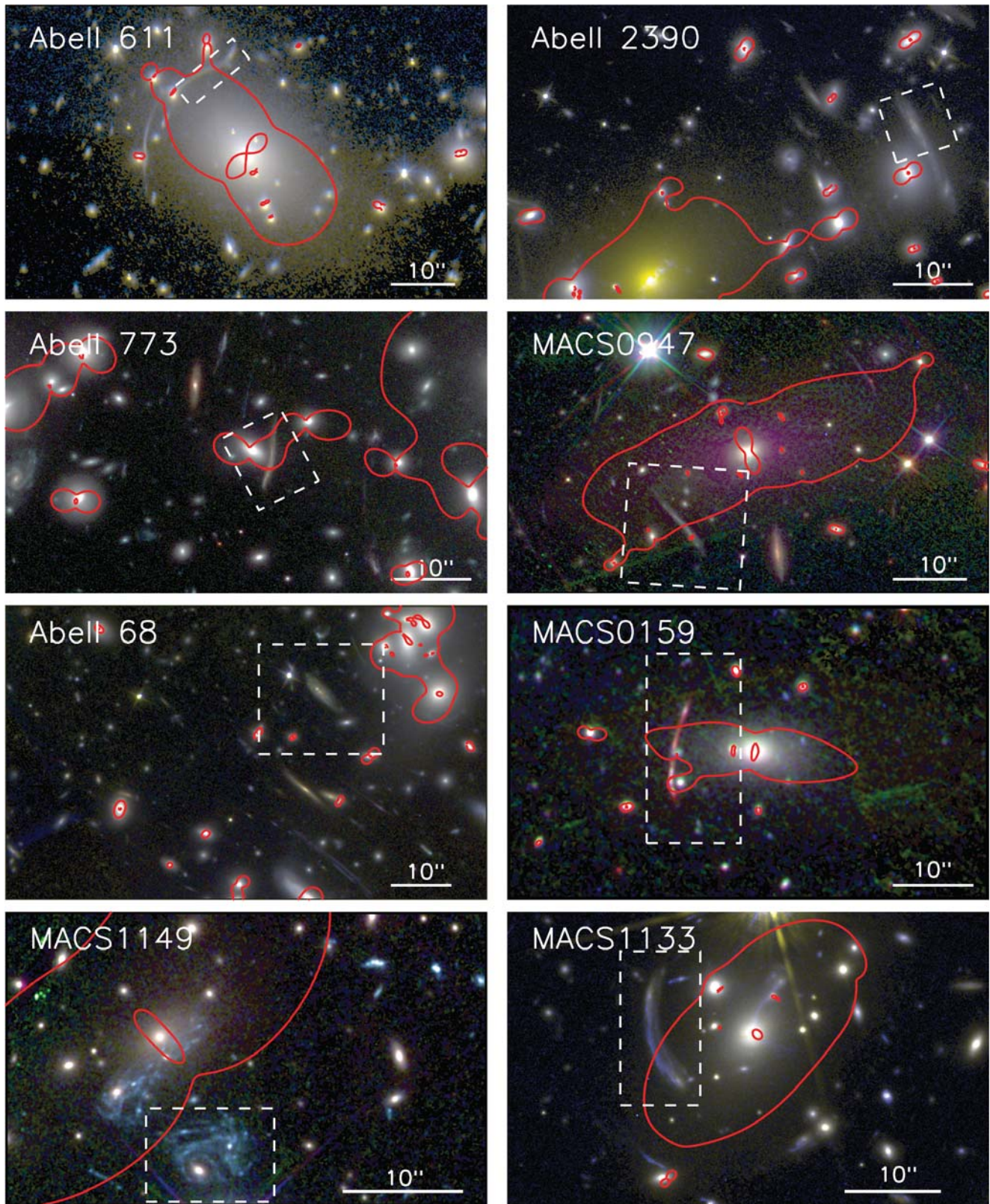
Figure 1. *HST*/ACS and WFC3 three-colour images of the observed clusters with the critical line at the redshift of the target arc overlaid, showing the positions of the target arcs. The arcs are contained within the white dashed boxes which denote the regions extracted in Fig. 2.

each image was checked by visual inspection and any foreground sources and defects masked. The resulting luminosities were then compared to the published values and found to agree to within ∼20 per cent.

We convert Hα luminosity to SFR using the Kennicutt (1998a) prescription, corrected to a Chabrier (2003) IMF, which reduces the SFR by a factor of 1.7×. As we do not have constraints on the dust extinction, we adopt an estimate of $A_{H\alpha} = 1$ in all
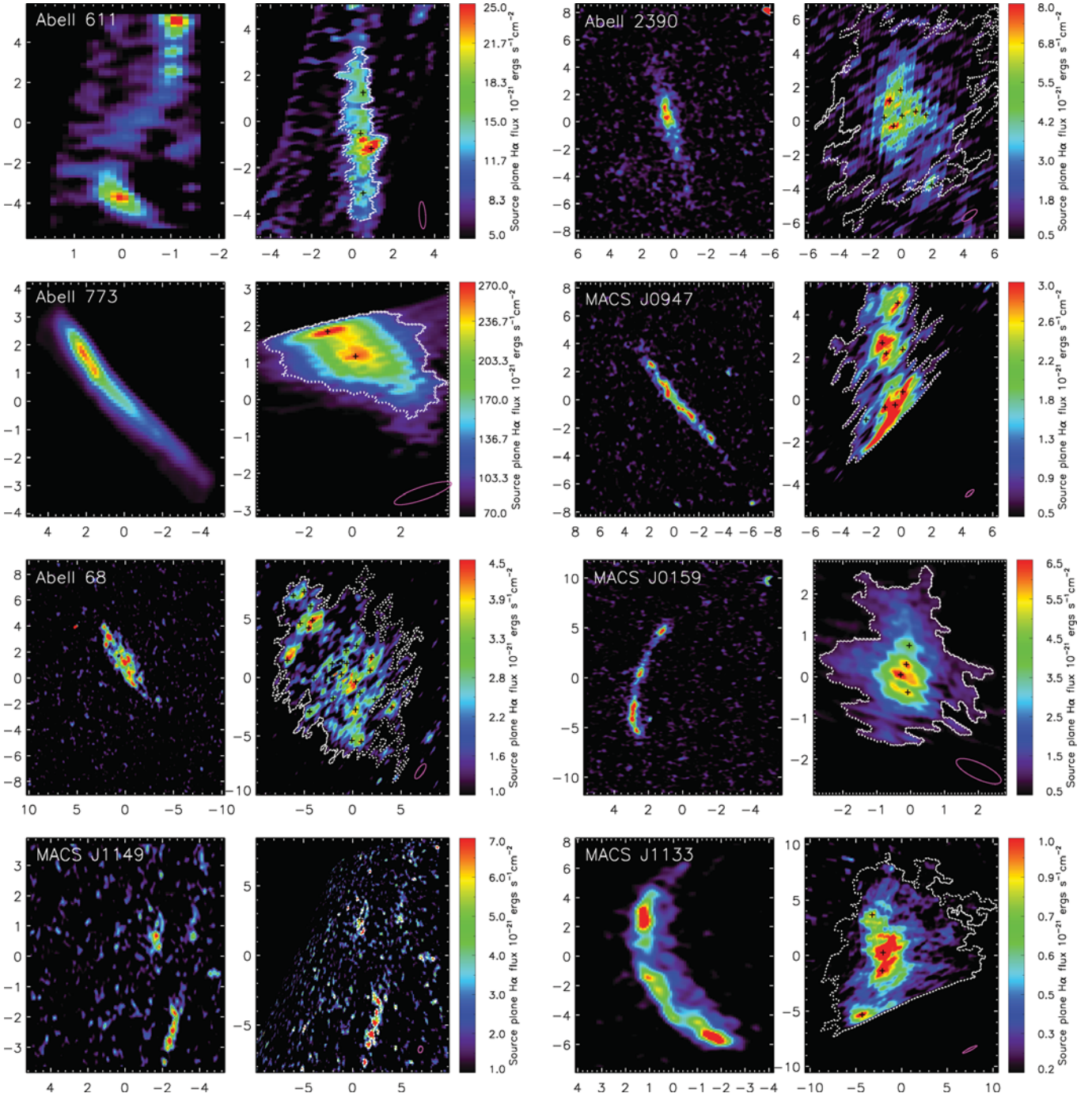
Figure 2. Hα excess images in the image plane (left) and reconstructed in the source plane (right). The image scales are in arcsec in the image plane and in kpc in the source plane. Identified clumps are indicated in the source plane images by black crosses, and the magenta ellipse shows the FWHM of the effective source plane PSF, as described in the text.

samples. This assumption is widely used in the literature although it is the subject of some disagreement. Garn et al. (2010) suggest a luminosity-dependent $A_{H\alpha}$ is more appropriate; were we to adopt their relation, we would obtain $A_{H\alpha} = 0.7$–1.6 with a median $A_{H\alpha} = 1.15$. However, we also note that recent work by Domínguez et al. (2012) suggests that galaxies with $L_{H\alpha} \lesssim 4 \times 10^{41}\,\mathrm{erg\,s^{-1}}$ may be consistent with having $A_{H\alpha} = 0$, and that above this threshold extinction increases in a luminosity-dependent way. Had we adopted this correction instead, the SFRs of the majority of our galaxies would be reduced by a factor of 2.5×. The exceptions are the three brightest $z \sim 2$ galaxies, in which the SFRs would

increase by factors of 1.3–1.8×, and the $z \sim 1$ galaxies Abell 68 and Abell 773; the former would be a factor of 1.8× lower, while the latter would be unchanged. Qualitatively, there is no significant impact on our results, as adopting either luminosity-dependent extinction relation would serve to increase the evolution we observe in Section 3.2.2. For simplicity and reproducibility, we adopt $A_{H\alpha} = 1$ throughout.

We define the sizes of the galaxies as twice the half-light radius. The half-light radius is determined using the continuum images to find the shape (i.e. the centre and major to minor axis ratio of an ellipse that best fits the galaxy), and then adjusting the semimajor axis
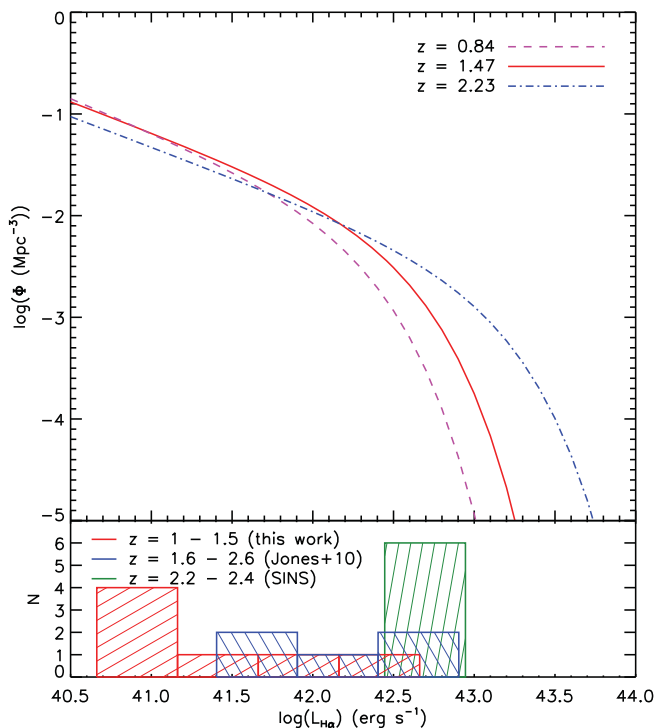
Figure 3. Intrinsic Hα luminosities of the high-z samples compared to Hα LFs from High-z Emission Line Survey (HiZELS; Sobral et al. 2012). Also shown is the range of Hα luminosities of the Förster Schreiber et al. (2011b) sample from the SINS survey at $z \sim 2$. The two lensed samples overlap in luminosity and are both at the faint end of the LF, with the median of the $z \sim$ 1–1.5 WFC3 sample lower than that of the $z = 1.6 - 2.6$ OSIRIS sample by a factor of 6.6×, while the unlensed SINS galaxies cover a range of higher Hα luminosities.

of the ellipse until it encompasses half of the total Hα luminosity calculated in the manner described above. The galaxy-averaged star formation surface density, Σ_{SFR}, is defined from the total luminosity enclosed within two half-light radii per unit area.

3 RESULTS AND ANALYSIS

3.1 The spatial distribution of star formation

A common theme in the recent literature is that high-redshift galaxies are 'clumpier' than galaxies in the local Universe. This concept originates from the frequent appearance of 'chain' galaxies in the high-redshift universe (e.g. Cowie et al. 1995; Elmegreen et al. 2004; Elmegreen & Elmegreen 2005). Even without looking at the properties of individual star-forming regions, it is interesting to compare the morphologies of the star-forming regions across the samples.

From visual inspection, it is clear that there are significant differences between the samples. In particular, the surface brightness distributions of the galaxies show distinct differences in the different samples. In Fig. 4, we show the fraction of star formation in pixels above a given Σ_{SFR} for the $z \sim 1$–1.5 and $z \sim 2$ samples, with the interquartile range of the thresholded SINGS sample shown for comparison.

To allow for the differing surface brightness limits of the samples, we only show star formation above a surface brightness of $\Sigma_{SFR} = 0.001\,M_\odot\,yr^{-1}\,kpc^{-2}$. This enables us to compare the star formation occurring in bright regions in a consistent manner. From the peaks

– i.e. the points at which the lines tend to zero – we can see that the samples are different, with the $z \sim 2$ galaxies having peak surface brightnesses of around an order of magnitude higher than the lower z samples. Similarly, the $z \sim 1$–1.5 sample is systematically brighter than the SINGS sample, with the exception of MACS J1133, which is similar to the fainter $z = 0$ galaxies, MACS J0947 which is similar to the median of the $z = 0$ sample, and Abell 773 which appears similar to the $z \sim 2$ galaxies.

As a statistical measure of the clumpiness of galaxies, we investigate using the Gini coefficient, G, which is used in economics to measure the inequality of wealth in a population (Gini 1912). It has values from 0 to 1, where at the extremes $G = 0$ for a completely uniform distribution, and $G = 1$ if there is only one non-zero value. Following Förster Schreiber et al. (2011a), we use it to quantify the distribution of flux in an image, so a value close to one indicates that the profile has a single peak (in the case of $G = 1$, all of the flux would be in a single pixel), a galaxy with multiple clumps would have a lower G, and at the extreme, a galaxy with completely uniform surface brightness would have $G = 0$.

In the $z \sim 1$–1.5 sample, we find a narrow range of $0.25 \leq G \leq 0.39$ with a median of $G = 0.34$. The $z \sim 2$ sample is marginally higher, with $0.42 \leq G \leq 0.56$ and a median of $G = 0.43$. The $z = 0$ SINGS sample has a similar median $G = 0.45$ but a much wider range of $0.05 \leq G \leq 0.82$, and the low-z (U)LIRGs have $0.38 \leq G \leq 0.85$ with the highest median $G = 0.70$. On the basis of the Gini coefficient there are no clear differences between the samples. Comparing the Gini coefficients with the visual appearance of the galaxies, the lack of distinction reflects the fact that a low Gini coefficient may arise from either a smooth distribution of star formation or from star formation that is concentrated into a large number of distinct clumps. Furthermore, we find no strong correlations between G and any of the properties of the galaxies. Clearly, to progress further we will have to compare the properties of individual clumps. In particular, we will show that the clump LF provides a good means of distinguishing different galaxy star formation morphologies.

3.2 Properties of star-forming clumps

3.2.1 Definition of clumps

Studies of H II regions or star-forming clumps have used a variety of methods to define and separate clumps from the background emission of the galaxy. Usually an isophote is defined at 3σ above the background noise (e.g. Gonzalez Delgado & Perez 1997; Jones et al. 2010). However, this method is clearly dependent on the noise properties of the image, and thus is problematic when comparing local and high-redshift observations. In particular, as high-redshift galaxy images tend to have high relative noise levels and low dynamic range, the choice of isophote tends to select only the brightest regions in the galaxy, neglecting any lower surface brightness clumps and underestimating their sizes.

An alternative is the IRAF task DAOFIND as employed by Förster Schreiber et al. (2011b), which is designed to locate point sources in images. However, we found that it did not perform well on our sample. This is likely to be because DAOFIND requires an expected size of features to look for. As the clumps of Förster Schreiber et al. (2011b) are largely unresolved, they were able to use the point spread function (PSF) of their observations as the expected size. As our clumps are resolved, the routine does not work reliably. For this paper we therefore use the 2D version of CLUMPFIND (Williams, de Geus & Blitz 1994), which uses multiple isophotes to define clumps.
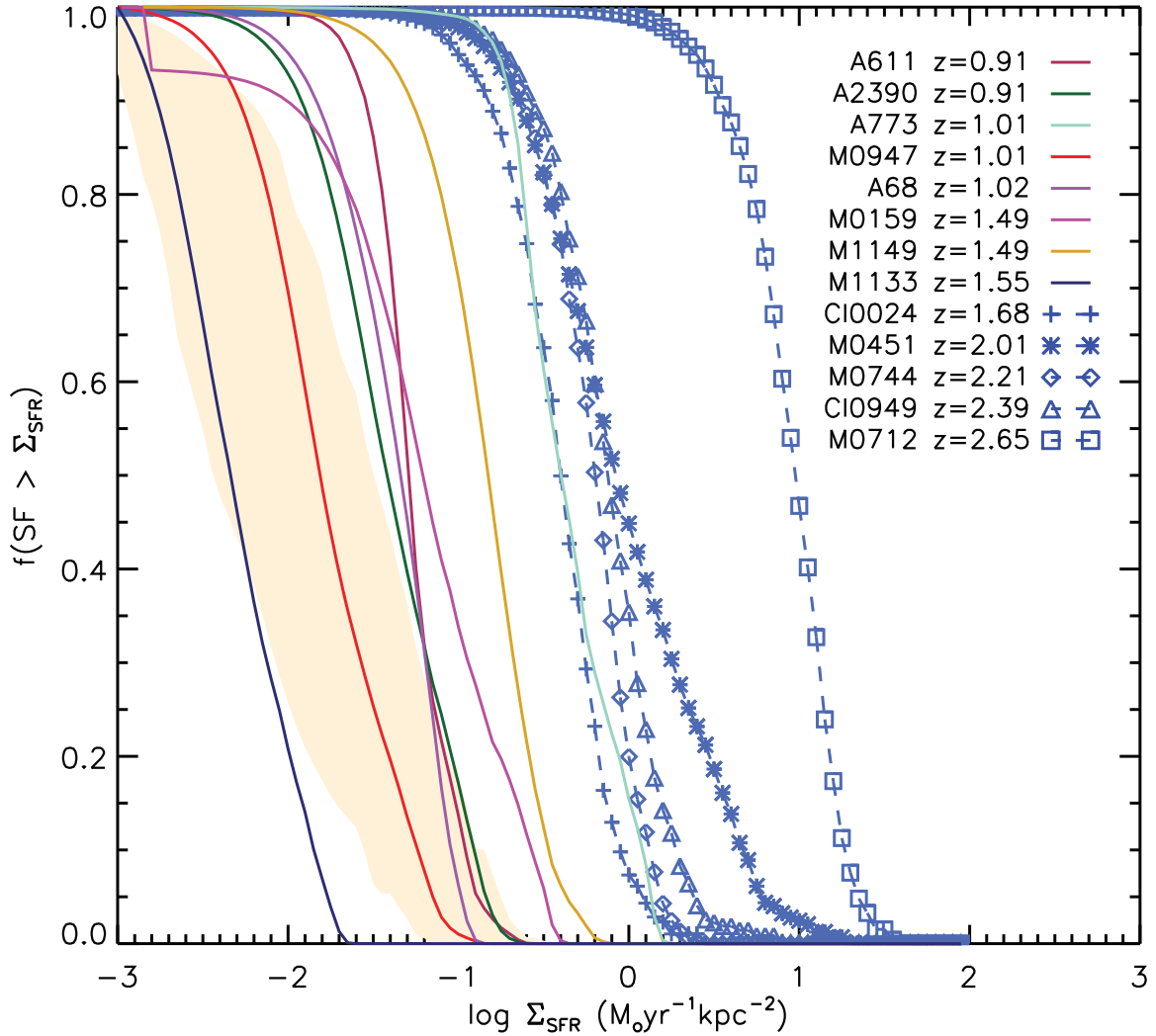
Figure 4. The fraction of star formation within each galaxy occurring above a given surface brightness, for the $z \sim 1$–1.5 and $z \sim 2$ samples. The shaded region is the interquartile range of the SINGS $z \sim 0$ sample. There are two galaxies, MACS J1133 and MACS J0947, from the $z \sim 1$–1.5 sample with similar surface brightnesses to the $z = 0$ sample, and the remainder are systematically brighter. The $z \sim 2$ sample has significantly higher surface brightnesses. Hence, there is clear evolution in the surface brightnesses of galaxies with redshift.

We defined the contour levels with respect to the rms noise in the image, starting at 3σ and increasing in 1σ intervals until the peak value of the image is reached. The data are first contoured at the highest level to locate clumps, and the algorithm then works down in brightness through the contour levels. Any isolated contours are defined as new clumps, while others extend existing clumps. If a contour surrounds one existing peak, they are allocated to that clump, and any which enclose two or more are divided using a 'friends-of-friends' algorithm. The advantages of this approach are that it enables a consistent clump definition to be applied to multiple data sets, lower surface brightness clumps are not excluded and there is no assumption made about the clump profile.

The clumps identified by CLUMPFIND were all confirmed by visual inspection to remove any source not associated with the target galaxy, of particular importance in the case of the SINGS images where foreground sources lie close to or overlap the target galaxies. The area A of the clump is then obtained from the number of pixels assigned to it, multiplied by the source plane pixel scale, and from this we define the effective radius $r = \sqrt{A/\pi}$. We only accept clumps where $2r$ is larger than the FWHM of the PSF, so all clumps are resolved.

Because of the manner in which clumps are 'grown', their sizes returned by CLUMPFIND tend to be larger than those obtained by other methods. As a comparison, we also fit a 2D elliptical Gaussian profile to each peak and measure the FWHM. A comparison of the clump radii found by the two methods is shown in Fig. 5. The rms difference between the two radii is $\sim$100 pc, and on average we find that CLUMPFIND outputs sizes 25 per cent higher than the FWHM. Wisnioski et al. (2012) note that sizes defined through isophotes can be unreliable due to the level of 'tuning' required to select an appropriate isophote level in a given galaxy. This is less significant with CLUMPFIND because this tuning is not required; the use of multiple isophote levels in all galaxies allows the levels to be defined in a consistent way across a large sample. We therefore find much lower scatter between the isophotal sizes output by CLUMPFIND and the clump FWHM than they do in their sample. Throughout this work, we use the CLUMPFIND size for all samples, and give error bars that encompass the FWHM of the clumps.

The sizes and Hα-derived SFRs of the $z \sim 1$–1.5 clumps are given in Table 2. We analyse these properties in comparison to the other samples below.
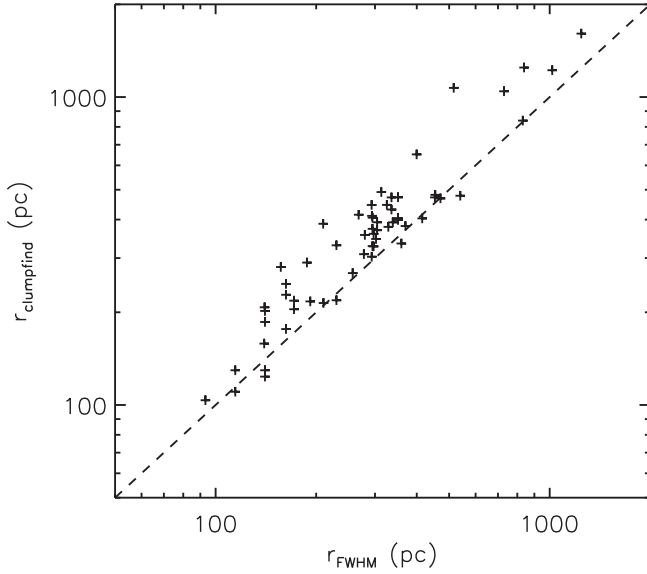
Figure 5. Comparison of the clump size $r_{clumpfind}$ output by CLUMPFIND with the size r_{FWHM} obtained by taking the FWHM of a 2D Gaussian profile fit. On average, CLUMPFIND outputs sizes 25 per cent larger than the FWHM. For consistency, we adopt the isophotal size output by $r_{clumpfind}$ in all samples.

3.2.2 Clump properties

One way of quantifying the 'clumpiness' of a galaxy is to consider the fraction of a galaxy's total Hα luminosity contained within clumps. We find medians of 31 per cent in SINGS, 36 per cent for the $z < 0.13$ ULIRGs, 50 per cent for the $z \sim 1$–1.5 sample and 68 per cent for the $z \sim 2$ sample. Thus, as expected, the higher z galaxies are clumpier than their local counterparts.

We now consider the properties of the clumps themselves, and first compare the Hα-derived SFR to the clump radius, as shown in Fig. 6. Locally, there is a well-defined relationship between these properties, as found by Kennicutt (1988) who found almost constant surface brightness in local H II regions, except in merging and interacting systems (Bastian et al. 2006). The situation at high-z, though, appears different; Swinbank et al. (2009) and Jones et al. (2010) found clumps with SFRs of $\sim 100\times$ higher at a given size than found locally, in systems with no evidence of interactions.

Fig. 6 is an updated version of one presented in Jones et al. (2010), where we have re-analysed the $z \sim 2$ and SINGS galaxies using CLUMPFIND so that clumps are defined consistently across all samples, and we have added the results from our new $z \sim 1$–1.5 data set and the $z < 0.13$ ULIRGs as well as the $z = 1$–2 results from SHiZELS (Swinbank et al. 2012) and WiggleZ (Wisnioski et al. 2012). We show lines of median surface brightness in the samples, and vertical offsets from these lines represent differences in the surface density of star formation, Σ_{SFR}, in the clumps. We will explore the relation of these offsets to global galaxy properties in Section 4.

We note that the clumps we identify in the SINGS galaxies are derived from images which have been degraded to comparable resolution to the high-z data, and we find the effect of this is to decrease the surface brightness by a factor of $\sim 2\times$, as the size increases more than the luminosity. The points in Fig. 6 move along the vector labelled 'A'. Defining clumps in the $z = 0$ sample in this way ensures the fairest possible comparison with the high-z data.

Upon re-analysis using CLUMPFIND, we find some lower Σ_{SFR} regions in the Jones et al. (2010) sample, but they all remain separated

Table 2. Properties of clumps identified in the $z \sim 1$–1.5 sample, determined as described in Section 3.2.1.

Clump	Radius (pc)	SFR ($M_\odot$ yr^{-1})
MACS J0947-1	350 ± 56	0.054 ± 0.010
MACS J0947-2	324 ± 22	0.0328 ± 0.0086
MACS J0947-3	384 ± 48	0.045 ± 0.012
MACS J0947-4	334 ± 39	0.0350 ± 0.0092
MACS J0947-5	318 ± 38	0.0339 ± 0.0089
MACS J0947-6	376 ± 6	0.0347 ± 0.0091
MACS J0947-7	311 ± 17	0.0261 ± 0.0068
MACS J0947-8	149 ± 9	0.0050 ± 0.0013
MACS J0159-1	402 ± 89	0.282 ± 0.060
MACS J0159-2	370 ± 77	0.203 ± 0.043
MACS J0159-3	530 ± 130	0.355 ± 0.076
MACS J0159-4	468 ± 13	0.170 ± 0.036
Abell 611-1	730 ± 180	0.370 ± 0.083
Abell 611-2	560 ± 160	0.181 ± 0.041
Abell 611-3	630 ± 140	0.200 ± 0.045
Abell 611-4	390 ± 59	0.065 ± 0.015
Abell 68-1	378 ± 26	0.081 ± 0.016
Abell 68-2	132 ± 8	0.0075 ± 0.0015
Abell 68-3	375 ± 24	0.076 ± 0.015
Abell 68-4	354 ± 25	0.070 ± 0.014
Abell 68-5	509 ± 31	0.114 ± 0.023
Abell 68-6	337 ± 33	0.062 ± 0.013
Abell 68-7	386 ± 61	0.099 ± 0.020
Abell 68-8	205 ± 42	0.0273 ± 0.0055
Abell 68-9	348 ± 44	0.069 ± 0.014
Abell 68-10	299 ± 89	0.066 ± 0.013
Abell 68-11	328 ± 31	0.057 ± 0.012
Abell 68-12	312 ± 15	0.0476 ± 0.0097
Abell 68-13	412 ± 60	0.100 ± 0.020
Abell 68-14	293 ± 16	0.0429 ± 0.0087
Abell 68-15	263 ± 5	0.0302 ± 0.0061
Abell 68-16	280 ± 50	0.0454 ± 0.0092
Abell 68-17	169 ± 7	0.0132 ± 0.0027
Abell 68-18	195 ± 33	0.0215 ± 0.0044
Abell 68-19	224 ± 6	0.0199 ± 0.0040
Abell 68-20	239 ± 51	0.0344 ± 0.0070
Abell 68-21	135 ± 5	0.0069 ± 0.0014
Abell 68-22	163 ± 23	0.0142 ± 0.0029
Abell 68-23	112 ± 2	0.00489 ± 0.00099
Abell 68-24	171 ± 31	0.0161 ± 0.0033
Abell 68-25	98 ± 5	0.00416 ± 0.00085
Abell 68-26	122 ± 8	0.0066 ± 0.0013
Abell 2390-1	352 ± 59	0.115 ± 0.025
Abell 2390-2	404 ± 68	0.136 ± 0.030
Abell 2390-3	409 ± 6	0.086 ± 0.019
Abell 2390-4	366 ± 26	0.067 ± 0.015
Abell 2390-5	463 ± 9	0.111 ± 0.024
Abell 2390-6	347 ± 13	0.059 ± 0.013
Abell 2390-7	470 ± 1	0.093 ± 0.020
Abell 2390-8	341 ± 73	0.069 ± 0.015
Abell 773-1	1040 ± 200	5.6 ± 1.3
Abell 773-2	1430 ± 180	9.6 ± 2.2
MACS J1133-1	1120 ± 100	0.118 ± 0.025
MACS J1133-2	890 ± 160	0.068 ± 0.015
MACS J1133-3	790 ± 280	0.057 ± 0.012
MACS J1133-4	835 ± 4	0.0334 ± 0.0072
MACS J1149-1	174 ± 34	0.084 ± 0.020

from the local relation by a factor of $\sim 100\times$. This confirms the large differences between the local and high-redshift population already noted by Swinbank et al. (2009) and Jones et al. (2010).

Our new $z \sim 1$–1.5 sample fits in between the SINGS and $z \sim 2$ samples, with the exception of the two regions from the most
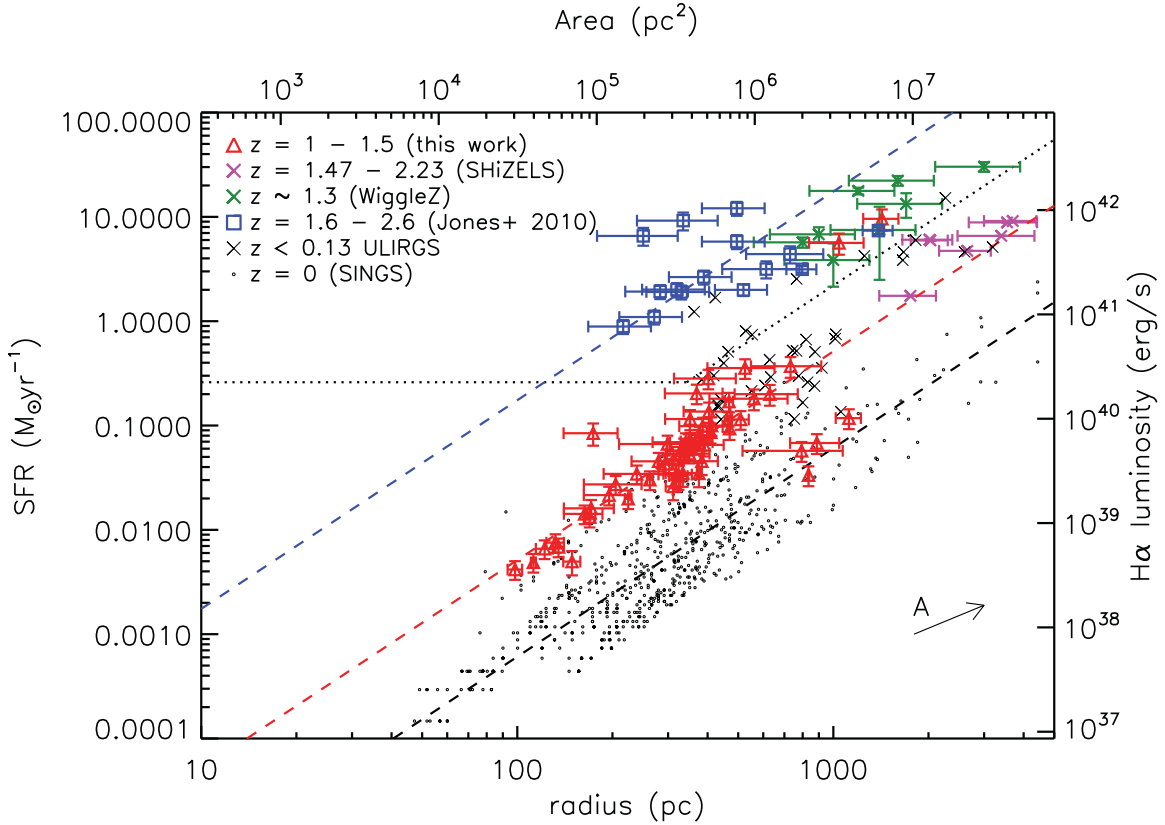
Figure 6. Hα SFR for extracted H II regions as a function of size, compared to the lensed $z \sim 2$ sample of Jones et al. (2010), high-z unlensed samples from SHiZELS (Swinbank et al. 2012) and WiggleZ (Wisnioski et al. 2012), low-z (U)LIRGs from Rodríguez-Zaurín et al. (2011) and the $z = 0$ SINGS galaxies (Kennicutt et al. 2003). SFRs are calculated using the Kennicutt (1998a) prescription adjusted for a Chabrier IMF with a dust extinction $A_{Hα} = 1$ in all samples, and the error bars of the high-z lensed sources are dominated by the uncertainty in the lensing magnification. Dashed lines show the median surface brightnesses in the SINGS, $z \sim 1$–1.5 and $z \sim 2$ samples. The black dotted line indicates the sensitivity limit of the $z \sim 2$ OSIRIS observations. The arrow indicates the effect of degrading the image resolution, as discussed in the text. The four lowest surface brightness clumps in the $z \sim 1$–1.5 sample come from one galaxy (MACS J1133), and the two brightest regions are from Abell 773, the most compact galaxy in the sample. The remaining galaxies have clumps with surface brightnesses in between those of the $z = 0$ and $z \sim 2$ samples, similar to local (U)LIRGs.

compact source Abell 773, which have Σ_{SFR} similar to the $z \sim$ 2 sample, and the four regions from MACS 1133, which are similar to $z = 0$ clumps. This indicates clear evolution in clump surface brightness, Σ_{SFR}, with redshift.

The surface brightness limit of the $z \sim 2$ data means that we cannot identify the low SFR clumps in that sample. We show a dotted line representing the lower limit at which we define clumps in the $z \sim 2$ galaxies. It is likely that there are additional clumps which lie below this limit and are undetected; however, such clumps make only a small contribution to the total SFR, as we shall discuss in Section 3.3.

Selection effects have no impact on the lack of high surface brightness regions in the lower redshift samples, however. The intense star-forming regions are clearly more common in high-z galaxies; they are found only in extreme systems such as the Antennae locally, but exist in all five of the $z \sim 2$ galaxies and one of the eight $z \sim 1$–1.5 sample.

As noted in Section 2, the $z \sim 2$ galaxies have 'normal' SFRs for their redshift, below the knee of the Hα LF. The offsets seen in the figure emphasize the importance of analysing clumps in terms of their surface brightness. This is even more evident if the clumps belonging to a single galaxy are examined separately. Rather than being distributed across the plot at random, individual galaxies form

a much tighter sequence with all the clumps sharing a common surface brightness, particularly in the low-redshift sample. Thus the spread in clump properties in Fig. 6 appears to be driven by *global* differences in the galaxies.

We therefore next compare the clump Σ_{SFR} to the properties of their host galaxies in Fig. 7. In the left-hand panel, we correlate the clump properties with the total SFR of the galaxy. For clarity, we plot the median clump Σ_{SFR} in each individual galaxy, and the error bars encompass the central 68 per cent of clumps within each galaxy (i.e. 1σ if they follow a Gaussian distribution). There is evidence for correlation between the clump Σ_{SFR} and the galaxy Hα luminosity (which we assume to be proportional to the total SFR); we find a Spearman rank correlation coefficient $\rho = 0.69$, representing a 5.8σ deviation from the null hypothesis of no correlation. This suggests that the star formation in the high-z sample follows a similar trend to the local sample, and that the differences seen in Fig. 6 may arise from the higher total SFRs of the high-redshift galaxies.

For the majority of the samples, an even stronger relation arises if we compare the clump Σ_{SFR} to the galaxy-averaged Σ_{SFR}. This is shown in the right-hand panel of Fig. 7, and has a correlation coefficient $\rho = 0.79$ with 6.6σ significance. The ratio of clump-to-average Σ_{SFR} can be thought of as a measure of the 'clumpiness' of the galaxy.
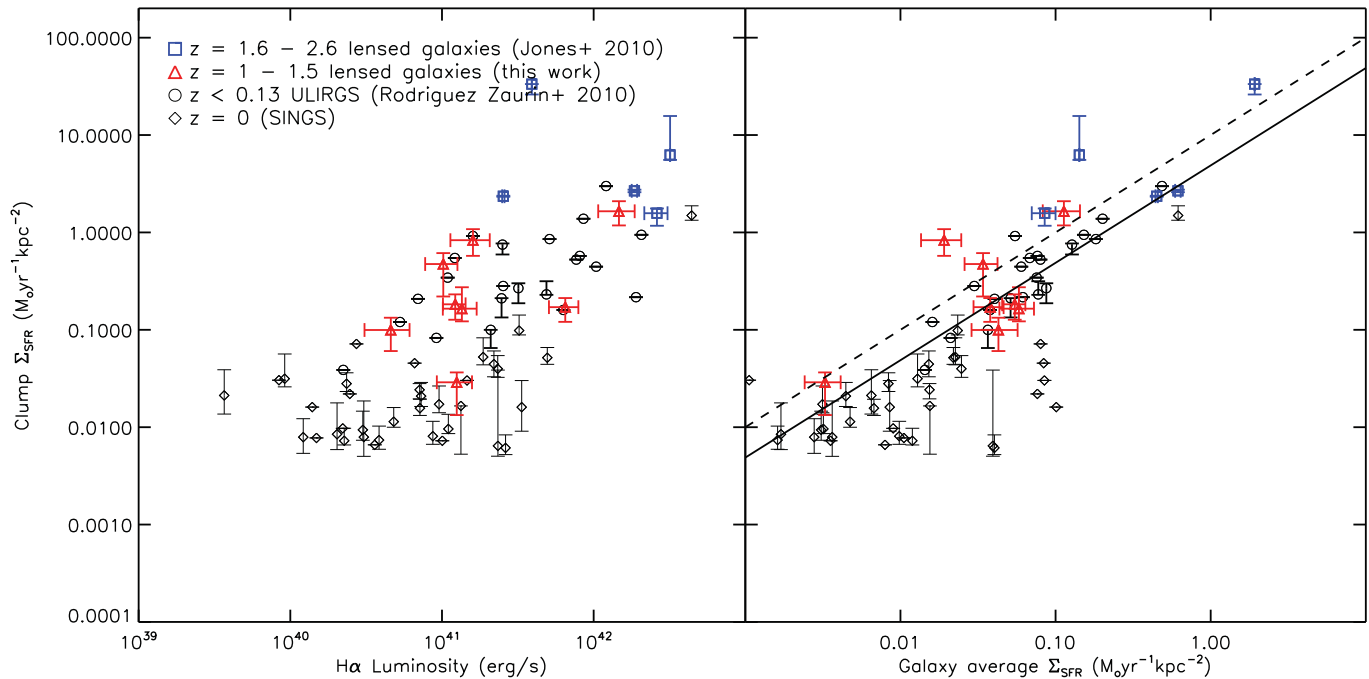
Figure 7. Comparisons between the star formation surface density Σ_{SFR} of star-forming clumps within each galaxy and the intrinsic Hα luminosity and galaxy-averaged Σ_{SFR}. The clump Σ_{SFR} shown is the median for each galaxy, with error bars encompassing the full range of Σ_{SFR} for all clumps within each galaxy. The solid line is the best fit to the data, and the dashed line illustrates the clump Σ_{SFR} expected from theory, discussed in Section 4. We find that both are correlated at the 5σ level, implying that we find more high Σ_{SFR} clumps at high redshift because there are more high SFR and Σ_{SFR} galaxies at this epoch.

We conclude that the properties of star-forming clumps in a galaxy are strongly dependent on the global Σ_{SFR} of the galaxy. Galaxies with higher overall Σ_{SFR} have higher clump surface densities and are correspondingly offset in the clump size–SFR relation. While this accounts for some of the differences seen in Fig. 6, it is also clear that there are more bright clumps in the higher redshift galaxies. We quantify this below.

3.3 H II region luminosity functions

A quantitative measure of the clump brightness is to construct a LF of H II regions. In the local Universe, the H II LF is presented in Kennicutt, Edgar & Hodge (1989) and Gonzalez Delgado & Perez (1997). They demonstrate that the LF can be fitted by a broken power law, or by a power law with an exponential break. In order to be consistent with our definitions of clump sizes, we re-analyse the local data in order to construct our own LF. The results are shown in Fig. 8. The left-hand panel of the figure shows the cumulative number of regions per galaxy as a function of Hα luminosity. The normalization of each bin takes into account the different surface brightness limit of the galaxies, with error bars computed from the Poisson error in counting regions. The slope of the power-law part of the mass function is ~ -0.75, so that although the LF appears steep in this representation, most of the total luminosity is contributed by the brightest H II regions.

Solid black points show the average of all SINGS galaxies. However, since we will be comparing the galaxies covering a range of luminosities and redshifts, we have separated the galaxies from the SINGS sample into three total Hα luminosity bins. At a fixed luminosity, galaxies with lower total emission have fewer regions, but the shape of the LF is similar. In order to emphasize the similarity of the mass function, we normalize each of the curves by the total

SFR of the host galaxies, and show this in the right-hand panel. The similarity of all the H II region LFs is now clear.

There is a striking similarity between the LF of the $z \sim 1$–1.5 sample and that of the highest SFR galaxies in the low-z SINGS sample. The excess of very bright regions ($L \sim 10^{41}$ erg s^{-1}) is down to one galaxy, Abell 773, which is the same compact galaxy for which we found the clump surface brightnesses to be more typical of the highest redshift galaxies. The low-luminosity slope of the LF tends also to be flatter than that seen in the low-redshift galaxies, but it is hard to quantify this difference without directly comparable surface brightness limits and is likely to be affected by unresolved regions which are excluded. In any case, these faint regions contribute little to the total flux.

In both panels, the H II region LF for the highest redshift galaxies is strongly offset from the relation seen in the low-redshift SINGS sample and from the sample at $z \sim 1$–1.5, but is similar to the low-redshift ULIRGs. Although the data do not probe the low-luminosity slope of the LF, these galaxies have much brighter regions than are seen at lower redshift. The right-hand panel emphasizes that this is not because they contain many more regions overall.

In order to compare our data to models of mass functions, we must relate the measured Hα luminosities to model clump mass, M. As an estimate, we use the Hα-derived SFR and adopt SFR $(M_\odot \text{ yr}^{-1}) = 4.6 \pm 2.6 \times 10^{-8} M_\odot$ (Lada, Lombardi & Alves 2010). This empirical relation is based on local molecular clouds and applies to the high-density gas where $A_K > 0.8$ mag. However, we note that this relation is consistent with the far-infrared-derived SFR and CO-derived gas masses of star-forming clumps reported in a lensed $z = 2.3$ galaxy by Swinbank et al. (2011), but clearly more high-resolution CO observations of high-z galaxies are required to confirm this. As a guide, we include this conversion on the upper axis of Fig. 8.
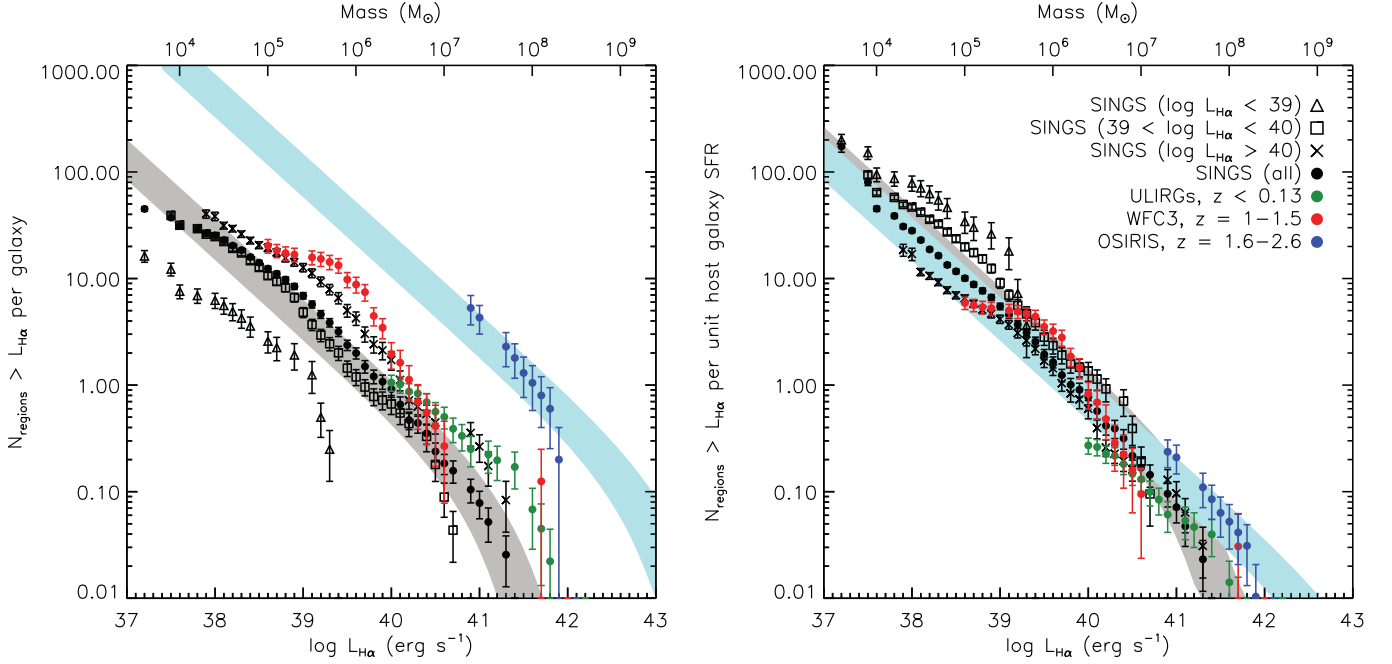
Figure 8. Cumulative LFs of H II regions in the SINGS, $z \sim 1$–1.5 and $z \sim 2$ samples, shown as a mean per galaxy (left) and normalized by total galaxy Hα luminosity (right). We plot the SINGS sample as a whole and subdivided into three luminosity bins. The shaded regions illustrate model predictions from the GMC mass functions of Hopkins, Quataert & Murray (2012) for Milky Way-like (grey) and high-z (blue) simulations. We find evolution in the H II region LF with redshift, which seems to be driven by the gas fraction of the disc.

The shapes of the LFs can be approximated by a power law with an exponential cut-off at some high luminosity or mass. The difference between the samples' LFs is then best described by a pure luminosity evolution, so that the cut-off shifts to higher luminosity/mass at higher redshift.

To demonstrate this, we include shaded regions representing a Schechter function of the form

$$N\,(>M) = N_0 \left(\frac{M}{M_0} \right)^{\alpha} \exp \left(\frac{-M}{M_0} \right), \tag{1}$$

where we adopt the median value of $\alpha = -0.75$ from Hopkins et al. (2012). The normalization N_0 is arbitrary, so we fit N_0 to the $z = 0$ data and then keep it fixed while allowing M_0 to vary in order to find best-fitting values of in the different samples. The best-fitting values are $M_0 = 4.6^{+3.1}_{-2.0} \times 10^7 \, \mathrm{M_\odot}$ at $z = 0$, $M_0 = 8.0^{+11.0}_{-4.3} \times 10^7 \, \mathrm{M_\odot}$ at $z \sim 1$–1.5 and $M_0 = 1.5^{+2.2}_{-1.0} \times 10^9 \, \mathrm{M_\odot}$ at $z \sim 2$, where the errors are found with a bootstrap method. We shade the best-fitting Schechter functions at $z = 0$ and $z \sim 2$ in grey and blue, respectively, in Fig. 8. The normalization of the model in the right-hand panel is obtained by summing the luminosities of the clumps. The result is in remarkably good agreement with our observations.

Not only do the highest redshift galaxies have H II regions that are higher surface brightness, but the characteristic luminosity of the regions is higher too. We suggest that the presence of high-luminosity regions may be a good operational definition of the clumpiness of a galaxy.

4 DISCUSSION

In the previous section, we presented an analysis of star-forming regions in galaxies at $z = 0$, $z \sim 1$–1.5 and $z \sim 2$. We find that the luminosities of the regions in $z = 1$ galaxies are similar to those

of bright ($L > 10^{40} \, \mathrm{erg \, s^{-1}}$) galaxies at low redshift, but the surface brightnesses are systematically higher. At higher redshifts, the properties of the galaxies change, with the galaxies having clumps that are both much higher surface brightness and shifted to higher total luminosities. This accounts for the qualitative impression that the most distant galaxies are 'clumpier'.

We also noted that the increase in the surface brightness of H II regions tracks the increase in the average SFR surface density, Σ_{SFR}, of the galaxies. The observations are consistent with the changing properties of the H II regions being driven by changes in the overall Σ_{SFR} of the galaxies. We can link the increase in the observed Σ_{SFR} to an increase in the gas surface density of these galaxies by assuming that the Kennicutt–Schmidt law holds at $z \sim 2$ as well as at $z = 0$. In this case, we have an emerging picture that the changes we see are likely driven by greater gas surface densities at higher redshift.

The connection between the increasing surface density of clumps and the greater peak brightness arises naturally from this picture (Hopkins 2012). The clump mass required for collapse on scale R from a turbulent ISM is given by the Jean's mass, M_{J}:

$$\rho_{\mathrm{c}} = \frac{3}{4\pi R^3} M_{\mathrm{J}} \approx \frac{9}{8\pi R^2 G} \sigma_{\mathrm{t}}(R)^2, \tag{2}$$

where $\sigma_{\mathrm{t}}(R)$ is the line of sight turbulent velocity dispersion. Assuming a turbulent velocity power spectrum $E(k)$, the velocity dispersion $\sigma_{\mathrm{t}}(R)$ for wavenumber $k = 1/R$ is

$$\sigma_{\mathrm{t}}^2 = kE(k) \propto R^{p-1}, \tag{3}$$

where $p \approx 2$ for supersonic turbulence appropriate to the ISM (Burgers 1974; Schmidt et al. 2009).

To determine the normalization of the relation, we assume that the clumps are located in a marginally unstable disc. We note that the available kinematic data for the $z \sim 2$ sample and for MACS J1149

support this assumption, as do larger surveys (Genzel et al. 2011); nonetheless, clearly this is uncertain without dynamical data for the entire sample. However, if we make the assumption that the galaxies are rotating discs with Toomre parameter $Q \approx 1$, we can relate the epicyclic frequency, κ of the disc to its scale height, h: $\kappa \approx \sigma_t(h)/h$,

$$Q = \frac{\kappa \sigma_t(h)}{\pi G \Sigma_0} \approx \frac{\sigma_t(h)^2}{\pi G \Sigma_0 h}. \tag{4}$$

Since the stability of the disc is a global phenomenon, we will associate Σ_0 with the average surface density of the star-forming disc, Σ_{disc}, and treat the quantities appearing in equation (4) as appropriate global disc averages. Since the disc is made up of both stars and gas, we must take an appropriate average of the surface densities in the two components. Following Rafikov (2001), and focusing on the largest unstable fluctuations, the appropriate combination of gas and star surface densities (denoted Σ_g and Σ_*) is

$$\Sigma_{disc} = \Sigma_g + \left(\frac{2}{1+f_\sigma^2}\right)\Sigma_*, \tag{5}$$

where $f_\sigma = \sigma_*/\sigma_t$ is the ratio of the velocity dispersion of the stellar component to that of the gas.

Assuming $Q \approx 1$, we can write

$$\sigma_t^2(R) = (\pi G \Sigma_{disc} h)\left(\frac{R}{h}\right)^{p-1} \approx \pi G \Sigma_{disc} R, \tag{6}$$

where we have used equation (3) to relate $\sigma_t(h)$ to $\sigma_t(R)$. Combining with equation (2) gives a critical density for collapse of

$$\rho_c(R) = \frac{9}{8}\Sigma_{disc}\frac{1}{R}. \tag{7}$$

Assuming that the cloud contracts by a factor of ≈ 2.5 as it collapses, the post-collapse surface density is

$$\Sigma_{cloud} \approx 10\rho_c R \approx 10\,\Sigma_{disc}. \tag{8}$$

Thus, for the turbulent power spectrum $p \approx 2$, the surface density of collapsed clouds is independent of radius and proportional to the surface density of the disc. The normalization of the relation follows from the collapse factor and the requirement that the disc is marginally stable. This model provides a good description of clouds in the Milky Way (Larson's laws) as discussed in Hopkins (2012), and predicts that the surface brightnesses of clouds should increase as the gas surface density (and thus overall average SFR surface density) increases. If we assume a constant Kennicutt–Schmidt law of the form $\Sigma_{gas} \propto \Sigma_{SFR}^{1.4}$ (Kennicutt 1998b), we can compare equation (2) to our data; we therefore overplot this line in Fig. 7 and find that it is in good agreement with the observations.

Moreover, the model predicts that the most massive clouds should increase in size with the average gas surface density. This follows from the marginal stability condition (equation 4), since density structures on scales greater than h will tend to be stabilized by disc rotation.

This can be demonstrated formally by examining the dispersion relation for a finite thickness disc (Begelman & Shlosman 2009). Hopkins (2012) shows that this leads to an exponential cut-off of the clump mass function above a mass

$$M_0 \approx \frac{4\pi}{3}\rho_c(h)h^3 = \frac{3\pi^3 G^2}{2}\frac{\Sigma_{disc}^3}{\kappa^4}, \tag{9}$$

where we have used equations (3) and (4) to express h as a function of Σ_{disc} and $\kappa = v_{disc}/R_{disc}$ (where v_{disc} is the disc circular velocity and R_{disc} is half-mass radius of the disc). Expressing κ in units of $100\,\mathrm{km\,s^{-1}\,kpc^{-1}}$ we obtain a normalization of

$$\frac{M_0}{M_\odot} = 8.6 \times 10^3 \left(\frac{\Sigma_{disc}}{10\,M_\odot\,pc^{-2}}\right)^3 \left(\frac{\kappa}{100\,km\,s^{-1}\,kpc^{-1}}\right)^{-4}. \tag{10}$$

We can check that this results in a reasonable value of M_0 in the Milky Way by using a gas surface density $\Sigma_{gas} \sim 10\,M_\odot\,pc^{-2}$ and a gas fraction of 10 per cent with $f_\sigma = 2$ (Korchagin et al. 2003) to obtain an effective $\Sigma_{disc} \sim 35\,M_\odot\,pc^{-2}$. With $\kappa = 36.7\,km\,s^{-1}\,kpc^{-1}$ (Feast & Whitelock 1997), this gives $M_0 \sim 10^7\,M_\odot$, in good agreement with the characteristic mass of the largest Galactic GMCs (Stark & Lee 2006).

Equation (10) shows that the mass cut-off depends strongly on the disc surface density – the higher the surface density, the more massive the clumps that are able to form. This trend can, however, be opposed by the stabilizing effect of angular rotational speed. For a fixed disc radius, a higher circular velocity tends to reduce the mass of the largest clumps.

For low-redshift galaxies, simple theoretical models suggest that $R_{disc} \propto v_{disc}$ since halo spin is weakly dependent on the halo mass (Mo, Mao & White 1998), and thus we should expect the dependence on the disc surface density to be the dominant trend controlling the cut-off clump mass. This is confirmed by analysis of the observed properties of galaxies. For example, Dutton et al. (2011) find

$$\frac{R_{disc}}{kpc} \approx 2.5 \left(\frac{v_{disc}}{100\,km\,s^{-1}}\right)^{1.2} \tag{11}$$

in the local universe. Combining this with the observed dependence of the disc rotation velocity on galaxy mass

$$\frac{M_*}{10^{10}\,M_\odot} = 0.25 \left(\frac{v_{disc}}{100\,km\,s^{-1}}\right)^{4.5}, \tag{12}$$

we obtain

$$\frac{\kappa}{100\,km\,s^{-1}\,kpc^{-1}} \approx 0.38 \left(\frac{M_*}{10^{10}\,M_\odot}\right)^{-0.04}, \tag{13}$$

which shows that κ is very weakly dependent on the galaxy mass, and the variation in the clump mass functions of local galaxies is driven by the disc surface density.

We also note that in a disc of constant circular velocity, κ scales with radial distance r as $\kappa \propto r^{-1}$, while the gas surface density profiles are shallow, with $\Sigma_{gas} \propto r^{-4/3}$ (Fu et al. 2010). Thus from equation (10) there is no dependence of M_0 on r; while the surface density is higher towards the centre of the galaxy, this is balanced by the higher rotational frequency. This explains the observations that clump properties appear to be driven by the global properties of their host galaxies rather than by local conditions, and this allows us to use disc-averaged values of κ and Σ.

We have no measurements of the gas contents of our samples, but dynamical information available for the $z \sim 2$ sample permits us to predict the cut-off mass in these galaxies from our model if we estimate Σ_{disc} from the dynamical mass. Using the measurements reported in Jones et al. (2010, see their table 2), we compute a cut-off mass ranging from 3.3×10^6 to $3.1 \times 10^9\,M_\odot$ for the $z \sim 2$ sample. The median value is $5 \times 10^7\,M_\odot$, approximately $5 \times$ higher than the Milky Way value. We therefore expect that the $z \sim 2$ sample should contain clumps of higher mass and luminosity, as observed. However, the uncertainty in the cut-off mass for the $z \sim 2$ sample is very large due to uncertainties in Σ_{disc} and κ, which prevents us from making a precise comparison of the cut-off mass in the different samples.

To understand how the clumpiness of galaxies evolves, we must therefore use simulations to estimate the evolution of their scaling relations. Dutton et al. (2011) present a simple analytic model that seems to describe the observational data well (Trujillo et al. 2006; Förster Schreiber et al. 2009; Williams et al. 2010). We use
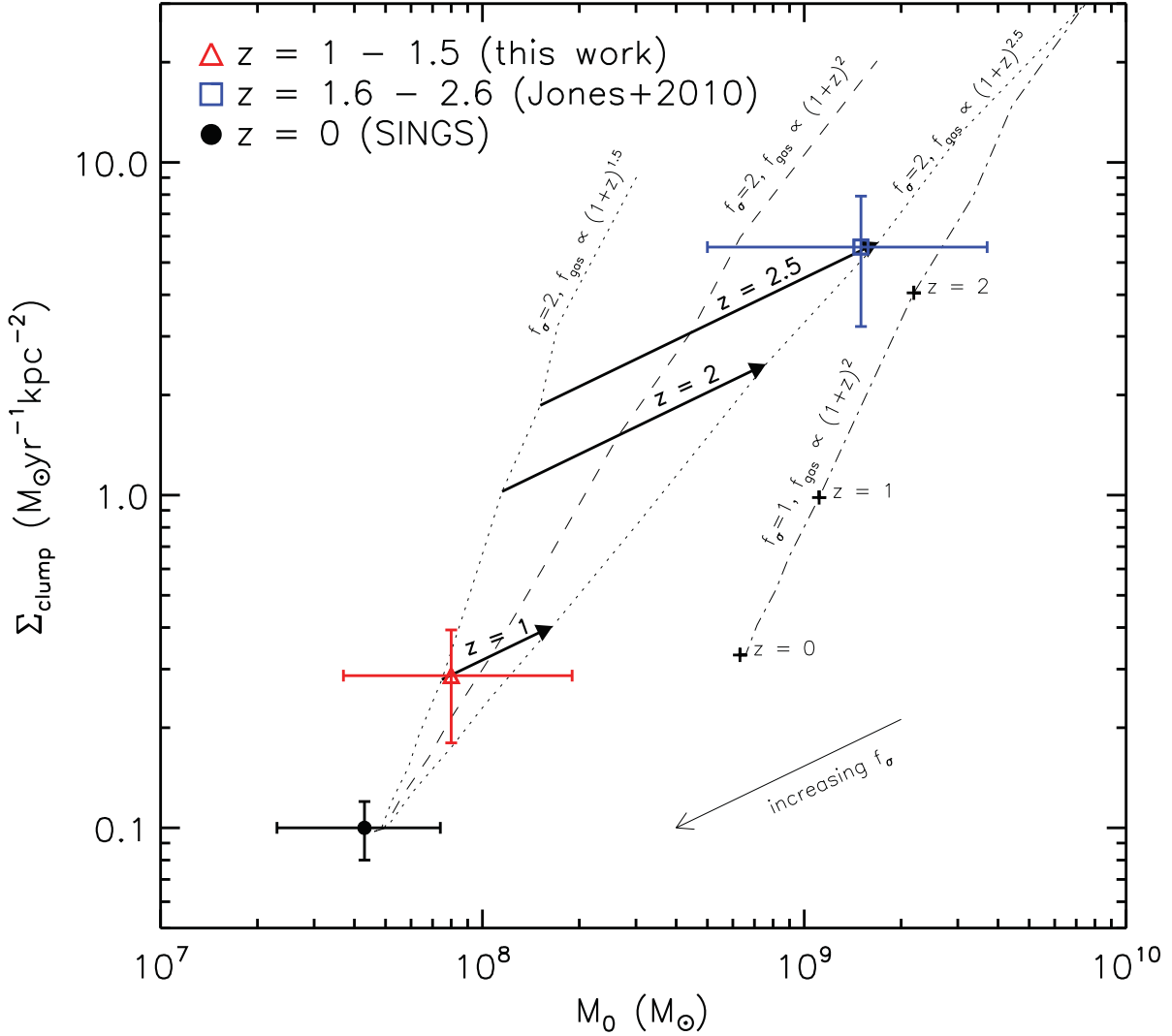
Figure 9. The evolution of cut-off mass M_0 and clump surface density Σ_{clump} in comparison with model predictions (equation 10). The model is strongly dependent on the assumed evolution of gas fraction with redshift; we show tracks for $f_{\mathrm{gas}} \propto (1+z)^{2 \pm 0.5}$ and the thick arrows show the effect of increasing the gas fraction. We also show a track for $f_\sigma = 1$ – i.e. assuming that the gas and stars have the same velocity dispersion. This makes the disc unstable on larger scales and would lead to higher mass clumps at low-z than are observed. The impact of this is reduced at higher z where gas dominates the disc dynamics. As f_σ increases, the points move in the direction of the arrow in the lower right-hand corner. The model provides a good fit to the data, demonstrating that larger, higher surface brightness clumps at high-z are a natural consequence of increasing gas fractions, which explains the observed morphologies of high-z galaxies.

their scaling relations for mass, size and rotational frequency with redshift in combination with equations (8) and (10) to predict how the cut-off mass and clump surface brightness should evolve with redshift. Fig. 9 illustrates this evolution for a gas fraction evolution of $f_{\mathrm{gas}} \propto (1+z)^{2 \pm 0.5}$ (Geach et al. 2011). The arrows show how altering the assumed gas fraction changes the model. This suggests that the changing clump properties are a natural consequence of increasing gas fractions dominating high-z galaxy dynamics. The high gas fractions probably arise from high gas infall rates at high redshift (Bournaud & Elmegreen 2009; Krumholz & Dekel 2010; Bournaud et al. 2011); however, our observations do not directly rule in or out cold flows. Our results merely require high gas fractions, and cold flows are a method of maintaining the gas supply. Crucially, we note that this effect is tempered by the more compact nature of galaxies, which leads to higher epicyclic frequencies that limit the collapse on larger scales. The need to include the κ term is apparent from our H II region LFs: without it, a factor of 10 increase in disc surface density would correspond to an increase in

clump luminosity of 1000×, and we do not observe such a large increase.

To summarize, we find that our simple theoretical model is in good agreement with the observations and suggests that the evolving 'clumpiness' of galaxies is a manifestation of the different cut-off mass of the H II region LF, which is driven by evolution in the gas fraction with redshift.

5 CONCLUSIONS

We have used *HST*/WFC3 to obtain narrow-band Hα imaging of eight gravitationally lensed galaxies at $z \sim 1$–1.5. The magnification provided by the lensing enables us to reach spatial resolutions in the source plane of 68–615 pc. In addition, to provide comparisons we have re-analysed the lensed $z \sim 2$ sample observed with Keck/OSIRIS by Jones et al. (2010), the Rodríguez-Zaurín et al. (2011) sample of $z < 0.13$ (U)LIRGs observed with VLT/VIMOS

and the Hα narrow-band imaging of the $z = 0$ SINGS survey (Kennicutt et al. 2003).

The high-z samples have 'clumpy' morphologies, dominated by a few large regions of high Hα luminosity, which we use as a proxy for the SFR. We have extracted star-forming clumps from the galaxies in each sample and examined their properties. The clumps follow similar SFR–size scaling relations in all samples, but the normalization of the relation exhibits systematic offsets to higher surface brightness at higher redshifts. The normalization appears to be approximately constant within a given galaxy, implying that this relation is driven by global galaxy properties.

On comparison with the properties of the host galaxies, we find that all samples follow approximately the same scaling relations between the clump surface brightness and both the host galaxy's total Hα luminosity, $L_{Hα}$, and its average surface density of star formation, Σ_{SFR}, and that they evolve along this relation in decreasing $L_{Hα}$ and Σ_{SFR} with decreasing redshift.

We have measured the LF of clumps in the samples, and shown that the $z \sim 1$–1.5 sample is similar to the higher $L_{Hα}$ members of the SINGS sample. When normalized by the host galaxies' total SFR, the SINGS and $z \sim 1$–1.5 samples can be fit by the same Schechter function, while the (U)LIRGs and $z \sim 2$ samples are offset horizontally. This shift can be explained by an increase in the cut-off mass of the H II region LFs of the (U)LIRGs and $z \sim 2$ discs.

We present a simple theoretical model which shows that the evolution in luminosity and surface brightness are connected, and are driven by the competing effects of disc surface density Σ_{disc} and the epicyclic frequency κ. Galaxies at high redshift tend to have higher Σ_{disc}, which increases the maximum mass of clumps that are able to form; however, this is tempered by the more compact nature of high-z galaxies, implying higher κ, which impedes collapse on the largest scales.

We have shown that this model is consistent with the evolution in clump properties seen in our data. We therefore conclude that the clumps observed in high-z galaxies are star-forming regions analogous to those found locally but with higher masses and surface brightnesses. As H II regions in the distant Universe are larger and brighter, they give rise to the 'clumpy' appearance. The increase in clump luminosity is driven primarily by increasing gas fractions at high-z. This clearly motivates further study with Atacama Large Millimeter/submillimeter Array (ALMA) to better quantify the evolution of gas properties in high-z galaxies.

REFERENCES

Bastian N., Emsellem E., Kissler-Patig M., Maraston C., 2006, A&A, 445, 471
Begelman M. C., Shlosman I., 2009, ApJ, 702, L5
Bournaud F., Elmegreen B. G., 2009, ApJ, 694, L158
Bournaud F., Elmegreen B. G., Teyssier R., Block D. L., Puerari I., 2010, MNRAS, 409, 1088
Bournaud F. et al., 2011, ApJ, 730, 4
Burgers J. M., 1974, The Nonlinear Diffusion Equation. Reidel, Dordrecht
Chabrier G., 2003, PASP, 115, 763
Cowie L. L., Hu E. M., Songaila A., 1995, AJ, 110, 1576
Dekel A., Sari R., Ceverino D., 2009, ApJ, 703, 785
Domínguez A. et al., 2012, preprint (arXiv:1206.1867)
Dutton A. A. et al., 2011, MNRAS, 410, 1660
Ebeling H., Edge A. C., Bohringer H., Allen S. W., Crawford C. S., Fabian A. C., Voges W., Huchra J. P., 1998, MNRAS, 301, 881
Ebeling H., Edge A. C., Henry J. P., 2001, ApJ, 553, 668
Ebeling H., Barrett E., Donovan D., Ma C.-J., Edge A. C., van Speybroeck L., 2007, ApJ, 661, L33
Ebeling H., Edge A. C., Mantz A., Barrett E., Henry J. P., Ma C.-J., van Speybroeck L., 2010, MNRAS, 407, 83
Elmegreen B. G., Elmegreen D. M., 2005, ApJ, 627, 632
Elmegreen B. G., Elmegreen D. M., Hirst A. C., 2004, ApJ, 612, 191
Elmegreen D. M., Elmegreen B. G., Ravindranath S., Coe D. A., 2007, ApJ, 658, 763
Elmegreen B. G., Elmegreen D. M., Fernandez M. X., Lemonias J. J., 2009, ApJ, 692, 12
Feast M., Whitelock P., 1997, MNRAS, 291, 683
Förster Schreiber N. M. et al., 2009, ApJ, 706, 1364
Förster Schreiber N. M., Shapley A. E., Erb D. K., Genzel R., Steidel C. C., Bouché N., Cresci G., Davies R., 2011a, ApJ, 731, 65
Förster Schreiber N. M. et al., 2011b, ApJ, 739, 45
Fu J., Guo Q., Kauffmann G., Krumholz M. R., 2010, MNRAS, 409, 515
Garn T. et al., 2010, MNRAS, 402, 2017
Geach J. E., Smail I., Moran S. M., MacArthur L. A., Lagos C. d. P., Edge A. C., 2011, ApJ, 730, L19
Genzel R. et al., 2006, Nat, 442, 786
Genzel R. et al., 2008, ApJ, 687, 59
Genzel R. et al., 2011, ApJ, 733, 101
Gini C., 1912, Memorie di metodologia statistica. Libreria Eredi Virgilio Veschi, Rome
Gonzalez Delgado R. M., Perez E., 1997, ApJS, 108, 199
Hopkins P. F., 2012, MNRAS, 423, 2016
Hopkins P. F., Quataert E., Murray N., 2012, MNRAS, 421, 3488
Jones T. A., Swinbank A. M., Ellis R. S., Richard J., Stark D. P., 2010, MNRAS, 404, 1247
Jullo E., Kneib J., Limousin M., Elíasdóttir Á., Marshall P. J., Verdugo T., 2007, New J. Phys., 9, 447
Kennicutt R. C., Jr, 1988, ApJ, 334, 144
Kennicutt R. C., Jr, 1998a, ARA&A, 36, 189
Kennicutt R. C., Jr, 1998b, ApJ, 498, 541
Kennicutt R. C., Jr, Edgar B. K., Hodge P. W., 1989, ApJ, 337, 761
Kennicutt R. C., Jr et al., 2003, PASP, 115, 928
Kneib J., 1993, PhD thesis, Université Paul Sabatier, Toulouse
Koekemoer A. M., Fruchter A. S., Hook R. N., Hack W., 2002, in Arribas S., Koekemoer A., Whitmore B., eds, The 2002 HST Calibration Workshop: Hubble After the Installation of the ACS and the NICMOS Cooling System. Space Telescope Science Institute, Baltimore, MD, p. 337
Korchagin V. I., Girard T. M., Borkova T. V., Dinescu D. I., van Altena W. F., 2003, AJ, 126, 2896
Krumholz M. R., Dekel A., 2010, MNRAS, 406, 112
Lada C. J., Lombardi M., Alves J. F., 2010, ApJ, 724, 687
Mo H. J., Mao S., White S. D. M., 1998, MNRAS, 295, 319

Pello R., Sanahuja B., Le Borgne J.-F., Soucail G., Mellier Y., 1991, ApJ, 366, 405

Rafikov R. R., 2001, MNRAS, 323, 445

Richard J. et al., 2007, ApJ, 662, 781

Richard J. et al., 2010, MNRAS, 404, 325

Rodríguez-Zaurín J., Arribas S., Monreal Ibero A., Colina L., Alonso-Herrero A., Alfonso-Garzón J., 2011, A&A, 527, A60

Sand D. J., Treu T., Ellis R. S., Smith G. P., 2005, ApJ, 627, 32

Schmidt W., Federrath C., Hupp M., Kern S., Niemeyer J. C., 2009, A&A, 494, 127

Smith G. P. et al., 2009, ApJ, 707, L163

Sobral D., Best P., Matsuda Y., Smail I., Geach J., Cirasuolo M., 2012, MNRAS, 420, 1926

Stark A. A., Lee Y., 2006, ApJ, 641, L113

Swinbank A. M., Bower R. G., Smith G. P., Wilman R. J., Smail I., Ellis R. S., Morris S. L., Kneib J., 2007, MNRAS, 376, 479

Swinbank A. M. et al., 2009, MNRAS, 400, 1121

Swinbank A. M. et al., 2011, ApJ, 742, 11

Swinbank A. M. et al., 2012, ApJ, submitted (arXiv:1209.1396)

Trujillo I. et al., 2006, ApJ, 650, 18

Williams J. P., de Geus E. J., Blitz L., 1994, ApJ, 428, 693

Williams R. J., Quadri R. F., Franx M., van Dokkum P., Toft S., Kriek M., Labbé I., 2010, ApJ, 713, 738

Wisnioski E., Glazebrook K., Blake C., Poole G. B., Green A. W., Wyder T., Martin C., 2012, MNRAS, 422, 3339

This paper has been typeset from a TEX/LATEX file prepared by the author.